Analysis of Design Alternatives of Actively Cooled RF Windows for MPEX

Joseph B. Tipton Jr., Arnold Lumsdaine, Michael C. Kaufman, Juan Caneses Marin, Jason Cook, Phil Ferguson, Richard Goulding, Dean McGinnis, Juergen Rapp, and the MPEX Team

[1]*Oak Ridge National Laboratory, Oak Ridge, TN, lumsdainea@ornl.gov*

ABSTRACT

The Materials Plasma Exposure eXperiment (MPEX) has been designed as a linear plasma divertor simulator in order to address Plasma Material Interaction (PMI) science for next generation fusion devices. It will have the capability to test neutron irradiated samples with plasma fluxes of greater than 10^{24} $m^{-2}s^{-1}$. It is expected to operate steady-state for up to 10^{6} s to consider PMI affects through reactor end-of-life. The conceptual design of MPEX was completed in 2019, with preliminary design beginning in 2020. The plasma source for MPEX is a helicon antenna, where the energized helical antenna sits outside of the vacuum in order to minimize impurities in the plasma. It is expected to receive up to 200 kW of continuous power, and so the antenna and the window must be actively cooled. The water-cooled copper antenna has been operated at full power on the proto-MPEX device (which is a test facility to demonstrate the plasma source and heating systems). The water-cooled window, however, is a novel component that must meet numerous competing requirements. It requires a low dielectric loss to allow the RF power to create the plasma within the vacuum boundary. It must be structurally robust to handle the significant heat flux from the plasma, and any heat from dielectric coupling. It must be compatible with the coolant (preferably water). It requires a vacuum seal that minimizes impurities into the plasma, and does not compromise the structural integrity of the window. Two window designs have been tested. Results from these tests, where temperatures are measured and heat-fluxes inferred from infrared

camera data, have been correlated with thermal-structural simulations. When these simulations are extrapolated to the full power steady-state heat fluxes which are expected in MPEX, the designs do not appear to have the necessary structural robustness. This study explores design alternatives for the MPEX helicon antenna window, presents analysis results for several of the alternatives, and shows a viable solution that satisfies the requirements for MPEX operation.

I. BACKGROUND AND MOTIVATION

Design efforts for a fusion power plant that demonstrates energy production are currently underway in many national and international programs[1-3]. Numerous privately funded fusion efforts present the possibility of a more agile movement towards fusion power demonstration[4-7]. A recent long-range plan from the US Department of Energy Fusion Energy Sciences Advisory Committee (FESAC) puts the United States fusion program on the path towards a Fusion Pilot Plant (FPP) in the 2040's[8]. In order to build a reliable, steady-state, operational fusion power

plant, a significant leap is required in understanding Plasma-Material Interaction (PMI) at high fluences. In particular, understanding the multivariate effects of neutron damage and high plasma fluence is necessary. The necessary high fluences are not within the capability of current toroidal devices, and thus steady-state linear test facilities have been proposed[9-12]. The Materials Plasma Exposure eXperiment (MPEX) is a linear divertor test facility that is currently in a preliminary design phase. Details on the MPEX design, and its science basis, can be reviewed in numerous references[13-17]. The purpose of MPEX will be to conduct high-fluence experiments, with the capability of handling a-priori neutron damaged samples[18]. MPEX proposes[15] to have ion fluxes $> 10^{24}$ $m^{-2}s^{-1}$ and ion fluences $> 10^{30}$ $m^{-2}s^{-1}$, with power fluxes on target of 10 MW/m^2. Steady-state plasmas will thus operate for up to 10^6 seconds. MPEX magnets will primarily be superconducting, with on-axis fields up to 2.4 T[19]. The design also allows for removal of the target from the vacuum chamber and removal, while still under vacuum, to a surface analysis station that is located away from the MPEX magnetic field, in order to study surface evolution during plasma exposure. As a steady-state device, the design of MPEX involves many engineering challenges not experienced in short-pulse devices, in terms of thermal management, active cooling, and considerations for the reliability, availability, and maintainability of the device.

MPEX uses a 200kW RF plasma source, where the water-cooled RF antenna sits outside of the vacuum[20-21]. As a non-contact source, this is intended to limit source-based impurities into the plasma. In order to operate in steady-state, the helicon window must be actively cooled as well. The conceptual window design has two nested cylinders with a water channel in-between. A schematic of the conceptual design of the MPEX helicon assembly is shown in Fig. 1.

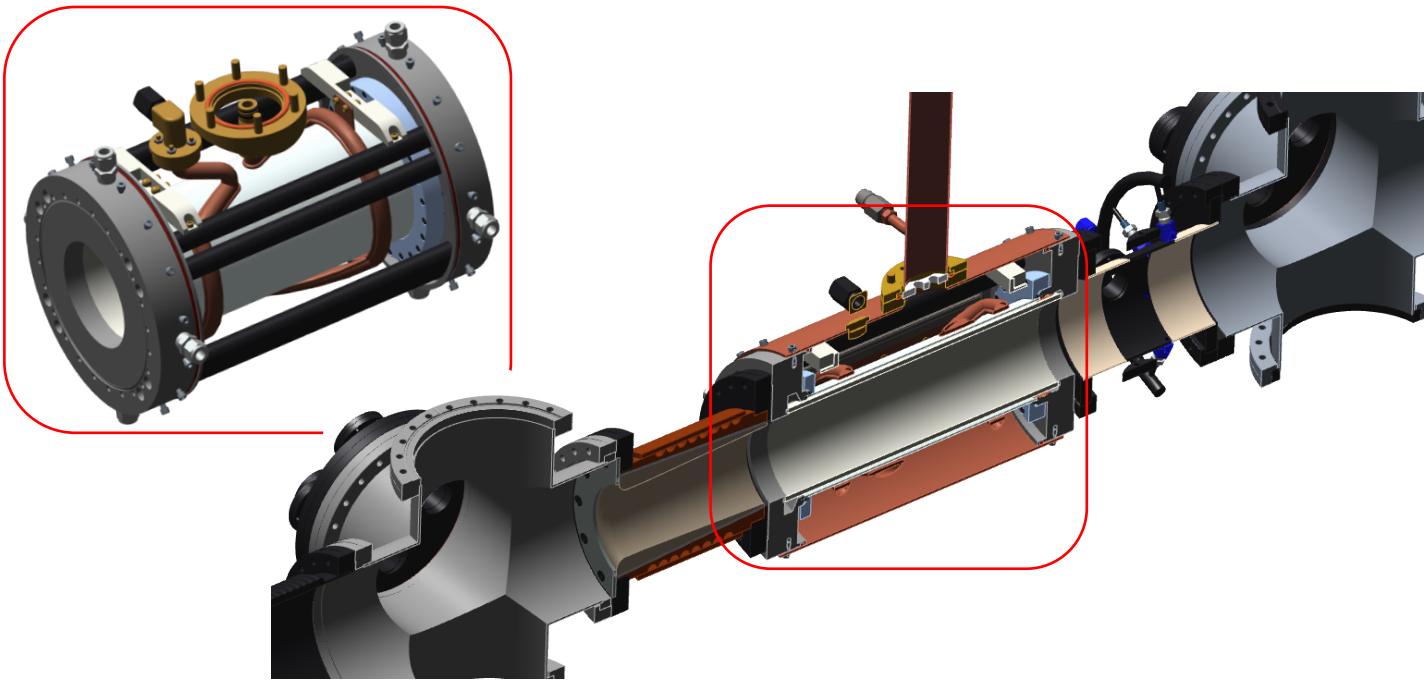

Figure 1: Cross-section of MPEX helicon antenna within the MPEX device (lower); full MPEX helicon assembly (upper left)

II. DESIGN OPTIONS FOR THE MPEX HELICON WINDOW

II.A. Requirements

A steady-state, high-powered helicon source has not been deployed before and is unique to MPEX. The design requirements specific to the helicon are:

1. The helicon antenna is required to produce plasmas with high electron densities in excess of 4×10^{19} m^{-3} in the source region.
2. The helicon antenna and power supplies shall operate at a fixed frequency of 13.56 MHz.
3. The system shall be configured to provide a coupled power of 175 kW to the MPEX plasma.
4. The helicon system shall operate in steady state to full power.

In particular, the requirement of continuous operation at high-power level presents thermal engineering challenges beyond those of previous pulsed experiments. Low dielectric window

materials (i.e. ceramics) are required. The engineering design solution consists of two ceramic windows with a coolant flowing through the annular channel in between. Another key challenge driving the design is the vacuum seal between the plasma and the coolant.

II.B. Design Choices and Previous Results

Table 1 summarizes the design history and options that have been tested and considered. Table 2 summarizes properties for three ceramic window options. The Proto-MPEX experiment used an aluminum nitride window (high thermal conductivity) and avoids the complexities of a coolant by using short pulse lengths along with natural convection[22]. The challenges of adopting an aluminum nitride window for MPEX are the difficulties in precisely manufacturing a cylinder of this size, and aluminum nitride's chemical reactivity to water. Applying a coating, or using a different coolant, would be possible, but would involve adding complexities to the device. The Controlled Shear De-correlation eXperiment (CSDX) at the University of California, San Diego operates in a steady-state regime with active cooling, but at lower power levels. CSDX was used to test a metal-to-ceramic braze with an alumina window. The low thermal conductivity and low thermal shock resistance of alumina presented a high-performance risk for MPEX. When scaled to MPEX power levels, previous results have shown thermal stresses in the window approach 90% of ultimate tensile strength (UTS)[21]. For a ceramic with highly stochastic fracture properties, this is not acceptable. In addition, the braze seal presents serious challenges to maintenance. Silicon nitride has significantly higher strength, higher thermal shock resistance, and is not chemically reactive with water. Thus, silicon nitride is chosen for the helicon inner window. (The outer window is quartz, as it does not have a significant thermal load). Sealing between the coolant and vacuum is still a challenge, and both elastomer and metal seals are being considered.

Table 1: Design choices – previous designs and testing

Facility	Window material	Vacuum seal	Coolant	Pulse length	Power
Proto-MPEX	Aluminum nitride	Elastomer	None	Seconds	200 kW
CSDX	Alumina	Elastomer	Water	Hours	10-20 kW
CSDX	Alumina	Metal-ceramic braze	Water	Hours	10-20 kW
MPEX design	Silicon nitride	Metal/ Elastomer	Water	Days	200 kW

Table 2: Properties of interest for potential ceramic window materials. Properties are taken from manufacturer published data.

Property	Alumina	Aluminum Nitride	Silicon Nitride
Thermal conductivity (W/m-K)	30	170	23
Flexural strength (MPa)	380	300	900
Thermal expansion coefficient ($x10^{-6}$ K^{-1})	8.2	5.2	2.8
Elastic modulus (GPa)	370	310	270
Thermal shock resistance (K)	97	140	857

III. ANALYSIS SETUP

III.A. Heat Flux Mapping

The Proto-MPEX experiment has tested RF plasma generation at configurations and power levels relevant to MPEX[23-24]. Infrared thermographic imaging techniques are capable of measuring temperatures on the inner surface of the AlN ceramic window[25]. The IR camera views

the surface of the AlN window through a ZnSe window and a stainless steel mirror at an angle of approximately 12 degrees relative to the horizontal. To properly perform the thermographic measurement, correct determination of the surface IR emissivity is required. The AlN window was heated uniformly and both thermocouple data and IR emission were recorded. The effective emissivity was chosen to match IR temperatures to thermcouple data.

A full mapping of the temperature field on the inner window surface is achieved by concatenating several IR camera images obtained at different orientations and swapping viewing ports. It takes six different images to obtain a near 360-degree view of the inner surface of the helicon window. Fig. 2(a) shows an example. Once the images are combined, grey body radiation assumptions are used to determine the thermograph, and a deconvolution algorithm is used to solve the associated inverse heat transfer problem and determine the heat flux mapping. Fig. 2(b) shows the heat flux mapping when extrapolated to the 175 kW coupled RF power anticipated in MPEX.

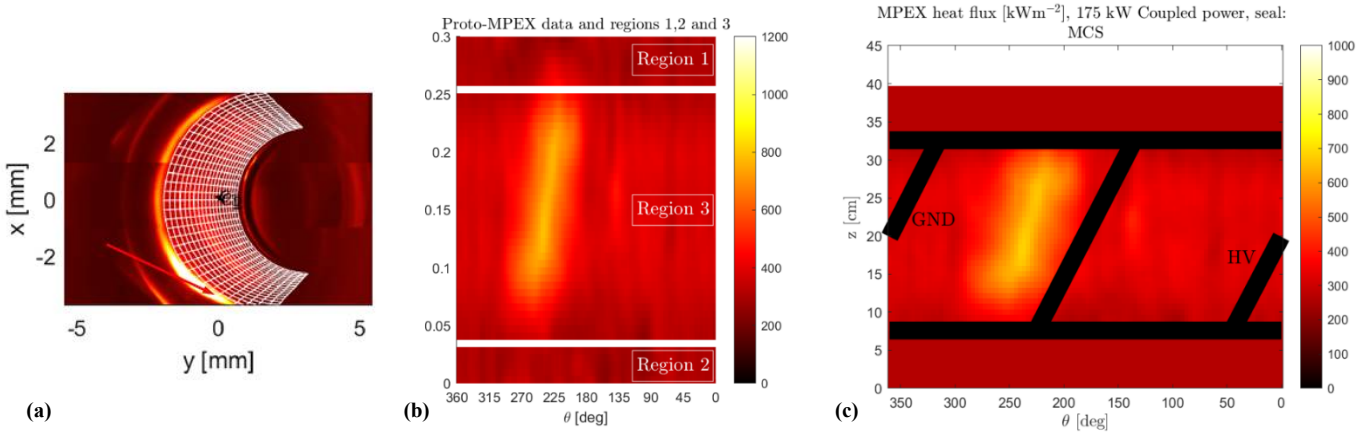

Figure 2: (a) An example IR image from Proto-MPEX showing a Cartesian grid mapping as well as a false hot spot due to reflection; (b) MPEX heat flux map extrapolated to 175 kW coupled power with regions interior and exterior to the antenna shown; (c) Resulting heat flux mapping for CFD simulation. Antenna straps are overlayed with high-volage "HV" and ground regions "GND" labeled.

Table 3: Dimensions of Proto-MPEX and MPEX helicon window and antenna. Note $L_w = L_1 + L_2 + L_a$.

Dimension	Symbol	Proto-MPEX	MPEX
Antenna length	L_a	0.22 m	0.25 m
Window length	L_w	0.3 m	0.398 m
Window inner radius	R_w	0.0626 m	0.0635 m
Edge to antenna length	L_1	0.0475 m	0.0722 m
Edge to antenna length	L_2	0.0325 m	0.0759 m

The starting point to create the heat flux maps for MPEX is the data shown in Fig. 2(b), which has been extrapolated to 175 kW coupled RF power. This data needs to be scaled, since the window and antenna dimensions of Proto-MPEX and MPEX are different (as described in Table 3). The first step is to divide the data in into the three regions shown. Region 3 represents the area enclosed by the RF antenna and MPEX heat flux in region 3 (q_3^{MPEX}) is calculated using the following operation:

$$q_3^{MPEX} = q_3^{Proto} \times \left(\frac{L_a^{Proto}}{L_a^{MPEX}}\right) \times \left(\frac{R_w^{Proto}}{R_w^{MPEX}}\right) \quad (1)$$

To produce the MPEX heat flux profiles for the regions 1 and 2, the average value of the Proto-MPEX heat flux in regions 1 and 2 is used and uniformly applied over the MPEX regions 1 and 2. The result is shown in Fig. 2(c) with the antenna straps overlayed. The peak heat flux is 683 kW/m^2 and the total heat load is 51.5 kW. ANSYS® CFX® then interpolates this data over the surface mesh of window. The uniform flux values in the L1 and L2 regions are extrapolated over the plasma facing surfaces of the flanges as well.

III.B. Thermofluid Modeling

The heat transfer and fluid flow are simulated using ANSYS® CFX® Version 19.2 software. This model includes the coolant (constant property water), flanges (TZM), vacuum seals, inner window (Si_3N_4), and outer window (Quartz). The vacuum seals between the inner window and flanges are either an EPDM elastomer or a Technetics Helicoflex® Delta spring energized metal seal. For heat transfer, the metal seal is approximated as solid nickel. Fig. 4 and 5 give an indication of the domains and discretization. The mesh is predominantly tetrahedral with 13.6 million control volumes. The mesh height near the wall is small enough to resolve the viscous sublayer ($y+ < 2$) which is recommended for accurate heat transfer predictions.

The bulk flow rate through the cooling channels is 75.7 L/min (20 gpm). The four inlets are each 11 mm diameter tubes which experience turbulent flow with a Reynolds number of $40x10^3$. The annular channel between the inner and outer windows has a cross-sectional area of $1.4834x10^{-3}$ m^2 with a gap of 3.3 mm. This also yields turbulent flow with a Reynolds number (based on the hydraulic diameter of 6.6 mm) of $6x10^3$. Mentor's Shear-Stress-Transport (SST) two equation model is used to model turbulent shear stress transport.

A mass flow rate equivalent to 75.7 L/min (20 gpm) is divided among the 4 inlets at 10°C and with 5% turbulence intensity. Walls are defined as no slip boundaries with a conservative interface heat flux to the surrounding solids. Outlets are defined as Neumann or zero-gradient with a specified average static pressure of 0 Pa. All solid external surfaces are defined as adiabatic except for the plasma facing surface on the inner window. Solid to solid interfaces are defined with conservative interface fluxes.

III.C. Structural Modeling

The structural analysis uses ANSYS® Mechanical™ Version 19.2 software and includes the flanges, inner window, support rods, and bolts. The solid domains are meshed with a tetrahedral method resulting in 6.6M elements and 10.2M nodes. The metal seals are difficult to model directly as they contain helical springs encased in a ductile jacket material. Instead, the seals are replaced with their equivalent sealing force on the flanges and inner window. Doing so effectively separates the window from the flange assembly as a separate body. Accordingly, the window is solved separately from the flange and support rods. Results from the two solutions are then combined to better understand relative displacements between the structures.

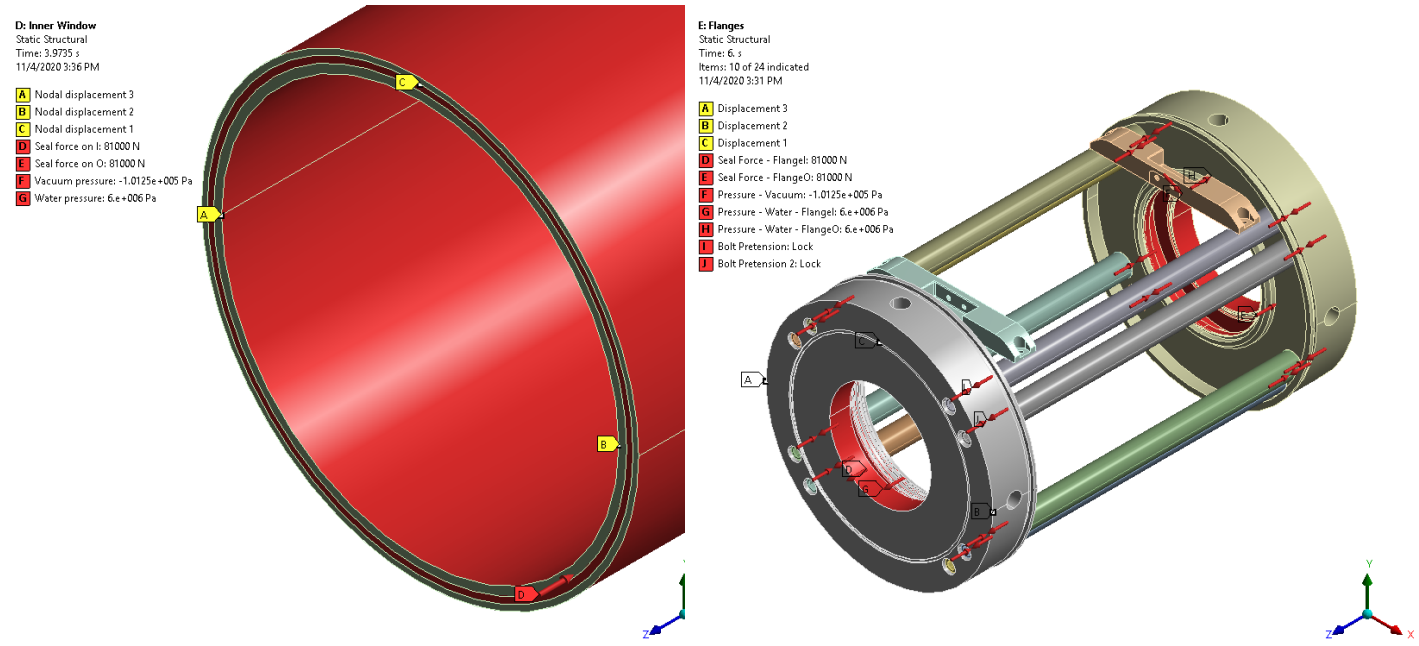

Figure 3: Structural boundary conditions and loads. The inner window and flange assemblies are modeled separately with equivalent seal forces applied.

Figure 3 shows the loads and boundary conditions on the inner window. Vacuum pressure is applied to the inside surface and water pressure is applied to the outside surface. The metal seals are not modeled directly, and the expected sealing force is instead applied on the contact surfaces.

ANSYS® Workbench® is used to import the ANSYS® CFX® thermal solution and map body temperatures to the window. Three vertex points from the CAD model are used for displacement boundary conditions. The nodes are at the inlet facing side of the window and are the minimum amount needed to avoid rigid body motion.

Figure 3 also shows the loads and boundary conditions on the flange structure. The flanges experience a vacuum pressure applied to the plasma facing lip surface. A static water pressure is applied to the interior passages in contact with coolant. The metal seals are not modeled directly, and the expected sealing force is instead applied on the contact surfaces in the groove. ANSYS® Workbench® is used to import the ANSYS® CFX® thermal solution and map body temperatures to the flanges. Note that the bolts and support rods are not included in the heat transfer model and are instead at uniform room temperature.

The 8 bolt heads on each flange are bonded to the mating flange surfaces. Similarly, the shanks of the bolts (smooth, with threads removed) are bonded to the support rods. Contact between the support rods and the flanges are modeled as frictional to allow the rods to deflect as the structure is loaded. Each of the 8 bolts receives a 12 kN pretension applied to the cylindrical face of the unbonded portion of the shank. The pretension is locked before other loads are applied.

Three vertex points from the CAD model are used for displacement boundary conditions. The nodes are at the outside surface of the inlet facing side of the flange and are the minimum amount needed to avoid rigid body motion.

IV. RESULTS

IV.A. Thermofluid Results

Figure 4 shows the domains in the analysis with a contour overlay of the mapped heat flux. Coolant streamlines with velocities are also included, showing a swirling flow through the annulus

region between the inner and outer window. The highest coolant velocities and pressure drop are in the inlet region and could be further optimized if the approximately 30 kPa pressure drop or erosion life is a concern. Generally speaking, the solution RMS residuals are able to reach below 1E-4 while the monitors of pressure drop and maximum temperature indicate a steady-state solution has been reached. Regions of poor convergence are shown to be in the recirculating region of the outlet flange manifold and away from areas of heat transfer concern.

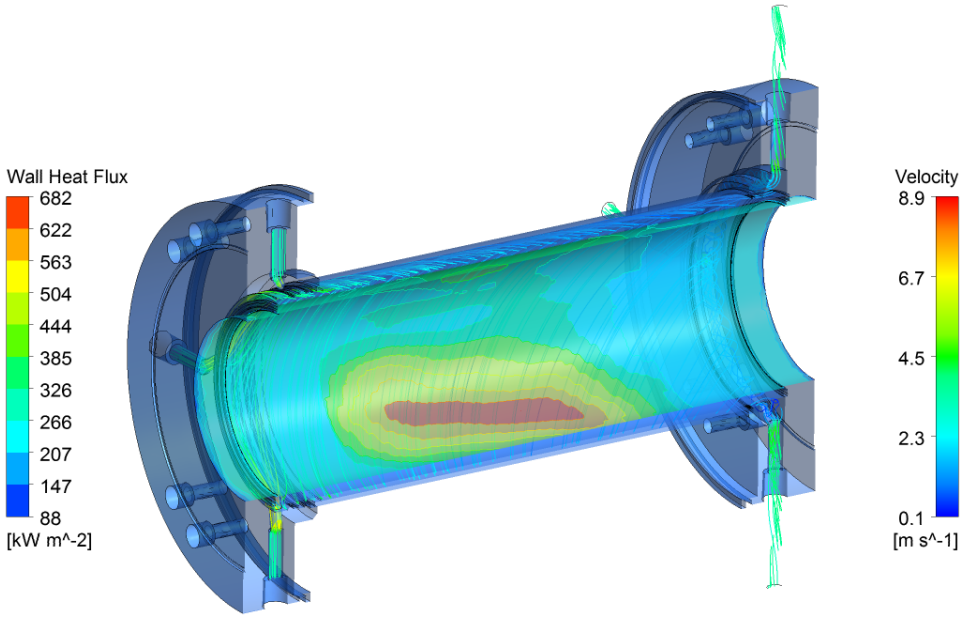

Figure 4: Cut plane view of helicon launcher domains for thermofluid modeling. Plasma heat flux contour plot and coolant velocity streamlines are overlaid.

Figure 5 shows temperature contour maps in a cross-section of the outlet region for both cases of a metal seal and a (deformed) elastomer seal. Table 4 compares maximum component temperatures for the two seal options. The seal temperatures are well within the 200°C limit for EPDM[26], and the maximum temperature is governed by contact with the inner window. Coolant maximum temperature shows localized boiling is not a concern.

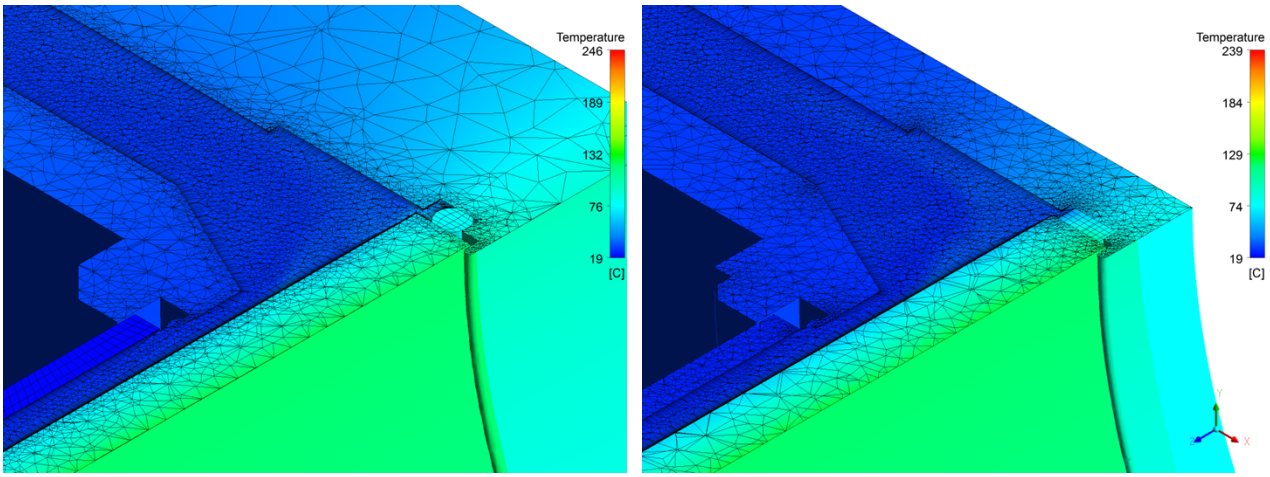

Figure 5: Cut plane views of temperatures at the outlet side of the helicon launcher assembly for a metal seal (left) and elastomer seal (right). Elastomer shown in deformed shape considering pressure loading. The flange is thicker for the metal seal to accommodate sealing load.

Table 4: Maximum component temperatures for the two vacuum seal models.

Seal Type	Metal	Elastomer
Flange (Inlet)	92 °C	91 °C
Flange (Outlet)	112	104
Outer Window	20	26
Inner Window	246	239
Seal (Inlet)	59	85
Seal (Outlet)	82	112
Peak Water Temp	102	93

IV.B. Structural Results

Structural results are presented only for the case of the metal seal as this presents the much higher load case and also requires careful attention to displacement. Figure 6 shows the maximum and minimum principal stresses on the inner window. Principal stresses are shown since the window is ceramic and would be expected to follow brittle failure theory. The area of maximum

plasma heating produces about 185 MPa maximum compressive stress on the interior surface and about 30 MPa tensile stress on the exterior surface. This tensile stress is an order of magnitude below the 1% probability failure stress of 350 MPa reported in C-Ring sample testing conducted at ORNL. Higher tensile and compressive stresses on the ends of the window have been ignored. It is felt these are an artifact of the vertex displacement boundary conditions as well as the loading condition which places the seal load on a portion of the face with no gradient to the unloaded surfaces.

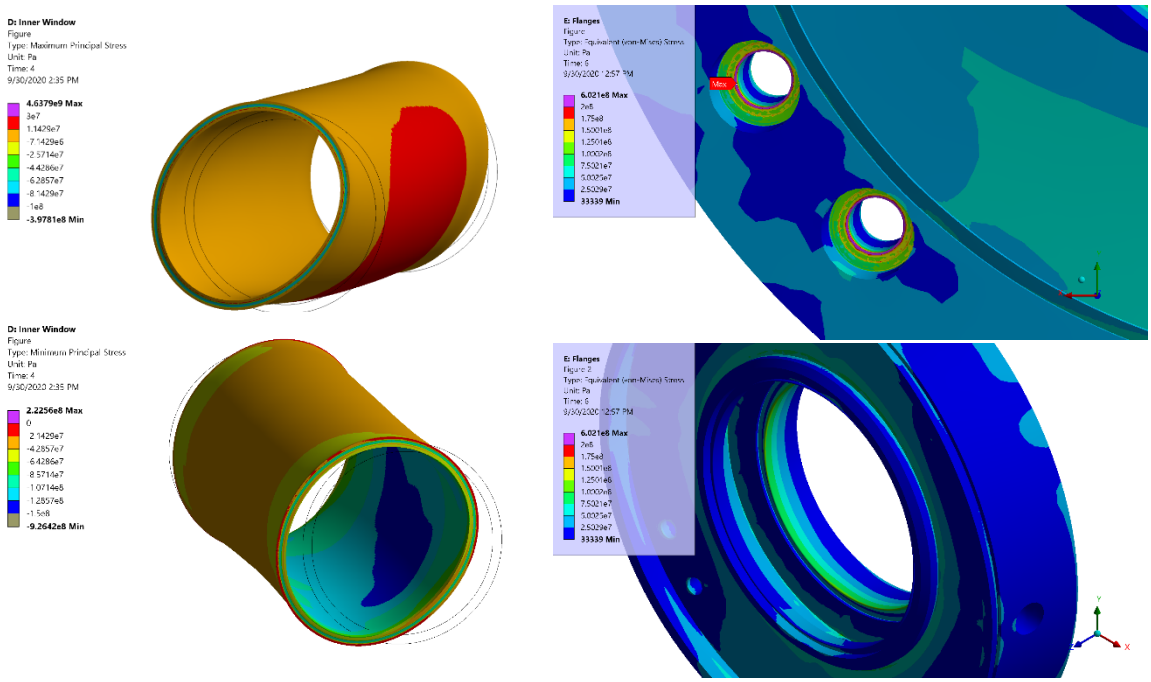

Figure 6: (L) Contour plots of principal stresses on the Si_3N_4 inner window with exaggerated deformation. (R) Contour plots of von Mises stress field on the outlet TZM flange.

Figure 6 also shows the von Mises stress distribution on the flanges. Maximum stresses are below 200 MPa. This is neglecting high stress regions at the sharp corners corresponding to bonded contact surfaces that are deemed artificial from the applied boundary conditions.

To explore displacement limitations of the metal seal, window axial deflection is determined using the top and bottom areas of seal contact which correspond with the deflection extremes. Flange axial deflection is also determined using the top and bottom areas of the seal groove which correspond with the deflection extremes. The CAD model begins with all surfaces in their nominal position. Application of the equivalent metal seal force causes the flange and window to move 65 μm apart on each end. Accordingly, the support rods on the actual assembly would need to be shortened 130 μm to ensure proper positioning of the flange and window with the properly seated metal seal.

With the additional loads (vacuum, water pressure, and thermal expansion) the window expands outward 47-57 μm while the flange deflects outward only 13 μm. This indicates that 34-44 μm of additional compression will develop on each seal. In reality, this will increase the seal force on components which has not been modeled. Assembly of the actual device should also ensure adequate gap between the window and flange to accommodate this expected additional compression.

This analysis has treated bolts and support rods as TZM and has not considered thermal expansion effects. Stainless steel will be a more practical material for these components. Cooling on the support rods might be needed to avoid thermal expansion.

V. CONCLUSIONS AND FUTURE STUDIES

Several conclusions can be drawn with respect to the initial scope of these analyses:

1. The elastomer seal model experiences seal temperatures at or about 112°C. This is within the limits of EPDM (200°C). Leak rates for an EPDM seal should be tested

given the critical vacuum/water sealing function. The flange could be redesigned to accommodate a double-elastomer seal with differential pumping, if needed.

2. The metal seal model experiences seal temperatures (82°C) well below the limits of Helicoflex Delta seals (370°C). After sealing, the seals are expected to receive further compression under operating conditions on the order of 1-2 mil. Further analysis or testing should address the ability of the seals to tolerate this displacement as well as potential thermal expansion of the support rods.
3. The TZM flange temperatures are approximately 112°C or below. Stresses are a factor of 2.75 below the ultimate tensile strength.

ACKNOWLEDGEMENTS

This material is based upon work supported by the U.S. Department of Energy, Office of Science, Office of Fusion Energy Science under contract number DE-AC05-00OR22725.

REFERENCES

1. G. FEDERICI, et al, "DEMO design activity in Europe: Progress and updates," *Fusion Eng. Des.*, **136 (A)**, 729, (2018).
2. G. ZHUANG, et al, "Progress of the CFETR design," *Nucl. Fusion*, **59**, 112010, (2019).
3. S. KWON, et al, "Recent progress in the design of the K-DEMO divertor," *Fusion Eng. Des.*, **159**, 111770, (2020).
4. M. BINDERBAUER, et al, "Systems and methods for forming and maintaining a high performance FRC" U.S. Patent No. 10,440,806, (2019).
5. S. SEGANTIN, et al, "Exploration of a fast pathway to nuclear fusion: thermal analysis and cooling design considerations for the ARC reactor," *Fusion Sci. Technol.*, **76**, *1*, 45, (2020).

6. S. MCNAMARA and Tokamak Energy Team, "Tokamak Energy and the high-field spherical tokamak route to fusion power," **APS 2019**, BO8-014, (2019).
7. P. O'SHEA, et al, "Acoustically driven magnetized target fusion at General Fusion: an overview," *B. Am. Phys. Soc*., **61** (2016).
8. https://science.osti.gov/-/media/fes/fesac/pdf/2020/202012/DRAFT_Fusion_and_Plasmas_Report_120420.pdf (current as of Dec. 28, 2020).
9. "FESAC Report on opportunities for fusion materials science and technology research now and during the ITER era 2012 DOE/SC-0149," http://science.energy.gov/~/media/fes/pdf/workshop-reports/20120309/FESAC-Materials-Sciencefinal-report.pdf (current as of Dec. 28, 2020).
10. "Report of the FESAC Subcommittee on the Priorities of the Magnetic Fusion Energy Science Program 2013," http://science.energy.gov/~/media/fes/fesac/pdf/2013/Final-Report-02102013.pdf (current as of Dec. 28, 2020).
11. "Report on Science Challenges and Research Opportunities in Plasma Materials Interactions 2015," https://www.burningplasma.org/resources/ref/Workshops2015/PMI/PMI_fullreport_21Aug2015.pdf (current as of Dec. 28, 2020).
12. "National Academies of Sciences, Engineering, and Medicine. 2018. Final Report of the Committee on a Strategic Plan for U.S. Burning Plasma Research," p. 5-6, Washington, DC: The National Academies Press. doi: https://doi.org/10.17226/25331.
13. J. RAPP, et al, "The Development of the Plasma-Material Interaction Facilities for the Future of Fusion Technology," *Fusion Sci. Technol*., **64**, *2*, 237, (2013).

14. A. LUMSDAINE, et al, "Pre-Conceptual Design Activities for the Materials Plasma Exposure Experiment", *Fusion Eng. Des.*, **109-111**, 1714, (2016).
15. J. RAPP, et al, "Developing the science and Technology for the Material Plasma Exposure eXperiment," *Nucl. Fusion*, **57**, 102020, (2017).
16. J. RAPP, et al, "The Material Plasma Exposure eXperiment: mission and conceptual design," *Fusion Eng. Des.*, **156**, 111586, (2020).
17. J. RAPP, et al, "The Materials Plasma Exposure eXperiment (MPEX): Status of the physics basis together with the conceptual design and plans forward," *IEEE T. Plasma Sci.*, **48**, *6*, 1439, (2020).
18. R.J. ELLIS and J. RAPP, "Neutron-Irradiated Samples As Test Materials for MPEX," *Fusion Sci. Technol.*, **68**, *4*, 750, (2015).
19. R. DUCKWORTH, et al, "Conceptual design and performance considerations for superconducting magnets in the Material Plasma Exposure eXperiment," *IEEE T. Plasma Sci.*, **48**, *6*, 1421, (2020).
20. A. LUMSDAINE, et al, "Design and Analysis of an Actively Cooled Window for a High Power Helicon Plasma Source," *IEEE T. Plasma Sci.*, **47**, *1*, 902, (2018).
21. A. LUMSDAINE, et al, "Testing and analysis of steady-state helicon plasma source for the Material Plasma Exposure eXperiment (MPEX)," *Fusion Eng. Des.*, **160**, 112001, (2020).
22. M. SHOWERS, et al, "Power accounting in the helicon region of plasma discharges in the linear device Proto-MPEX," *Plasma Phys. Contr. F.*, **60**, *6*, 065001, (2018).
23. J. CANESES MARIN et al, "Differential pumping requirements for the light-ion helicon source and heating systems of Proto-MPEX," *Phys. Plasmas*, **25**, *8*, 083518 (2018); http://dx.doi.org/10.1063/1.5001519

24. J. CAUGHMAN et al., “Plasma source development for fusion-relevant material testing,” *J Vac. Sci. Technol. A*, **35**, 03E114 (2017); https://doi.org/10.1116/1.4982664
25. J. CANESES MARIN et al, “Characterizing the plasma-induced thermal loads on a 200-kW light-ion helicon plasma source via infra-red thermography,” *Plasma Sources Sci. T.,* (submitted for publication).
26. Parker O-Ring Handbook (ORD 5700), Parker Hannifin Corporation, Cleveland, OH (2018).